Metal-insulator transition and anomalous lattice parameters changes in Ru-doped VO_2

Xin Gui and Robert J. Cava*
Department of Chemistry, Princeton University, Princeton New Jersey 08540, USA

(Received 26 March 2022; accepted 15 June 2022; published 15 July 2022)

VO_2, of interest for decades due to both its phenomenology and its potential applications, has a monoclinic distortion of the rutile crystal structure at ambient temperature that is coupled to its metal-insulator transition. In contrast, RuO_2 has three electrons more per formula unit, is a metallic conductor, and has an undistorted rutile structure. Here, we report a systematic study of Ru-doped VO_2 ($V_{1-x}Ru_xO_2$, $0.01 \leqslant x \leqslant 0.9$), generally characterizing its crystal structure, magnetic and electronic properties, and heat capacity. The composition-dependent Wilson ratio is determined. We find that an unusually high Ru doping value (80%, $x = 0.8$) is required to achieve a metallic state in $V_{1-x}Ru_xO_2$. No superconductivity was observed down to 0.1 K in the metallic materials. We propose a possible understanding for how the insulating state can exist in $V_{1-x}Ru_xO_2$ at high Ru contents.

DOI: 10.1103/PhysRevMaterials.6.075005

I. INTRODUCTION

Vanadium dioxide (VO_2) undergoes a metal-insulator transition (MIT) when cooled through ~340 K, accompanied by a structural phase transition from a high-temperature tetragonal structure to a low-temperature monoclinic structure [1,2]. It has been widely investigated for decades due to this MIT, which is of strong fundamental interest [3–29], and due its potential in applications, which include optical switches [30], strain sensors [31], and gas sensors [32]. The MIT in VO_2 has been investigated by heating [4], doping [21,22,24,25,33], application of electric fields [34–36], and structural stress [14,37,38], for example. Not without controversy, both the Peierls state, which involves spin-singlet formation by electrons on neighboring V atoms, and the Mott-Hubbard state, for which electrons attempting to occupy the same site undergo coulombic repulsion, have been proposed as needed to explain the insulating state [5,11,16–20,39–41].

Here, we report a systematic study of how Ru substitution for V in VO_2 affects its crystal structure, magnetic and electronic properties, and heat capacity. The lattice parameters of Ru-doped VO_2 have been previously reported but without any characterization of its physical properties [42]. Since Ru has three more valence electrons than V, it can be imagined that the metallic state should be easily induced by doping a small amount of Ru into VO_2. However, our results show that the insulating phase in VO_2 does not become metallic until a high doping value of 80%, i.e., that $V_{0.2}Ru_{0.8}O_2$ is a metal while $V_{0.3}Ru_{0.7}O_2$ is not. We propose a pathway for how Ru doping can affect the magnetic and electronic properties in $V_{1-x}Ru_xO_2$.

II. EXPERIMENT

A. Preparation of polycrystalline samples of $V_{1-x}Ru_xO_2$

Polycrystalline $V_{1-x}Ru_xO_2$ ($0 < x < 1$) was synthesized by using a high-temperature solid-state method. VO_2 (99%, powder, Beantown Chemical) and RuO_2 (99.9%, powder, Sigma-Aldrich) were used as starting materials as purchased. The mixtures of VO_2 and RuO_2 with appropriate stoichiometry were thoroughly ground and placed in alumina crucibles which were then sealed in evacuated quartz tubes. Two heat treatments at 950 °C for 2 d were carried out, with intermediate grinding. The final products were black powders and are resistant to air and moisture.

B. Phase identification

Powder x-ray diffraction (PXRD) characterization of the materials was carried out on a Bruker D8 Advance Eco diffractometer with Cu Kα radiation and a LynxEye-XE detector. The lattice parameters of $V_{1-x}Ru_xO_2$ were determined by using Rietveld fitting within the FULLPROF suite.

C. Physical property measurements

Magnetization measurements were performed using a physical property measurement system (Quantum Design PPMS) with a vibrating sample magnetometer. Here, M vs T data were collected in an applied field of 3000 Oe in the temperature range of 1.8–350 K and, when necessary, under various applied magnetic fields. The magnetic susceptibility was defined as M/H, where H is the applied magnetic field in Oe, and M is the measured magnetization in electromagnetic units. The four-probe method was employed to measure temperature dependence of resistivity. The samples for resistivity measurements were prepared by pressing $V_{1-x}Ru_xO_2$ powders and annealing them at 1000 °C for 12 h. The phase was not changed after this process, confirmed by PXRD. Heat capacity was measured using a standard relaxation method in

*rcava@princeton.edu

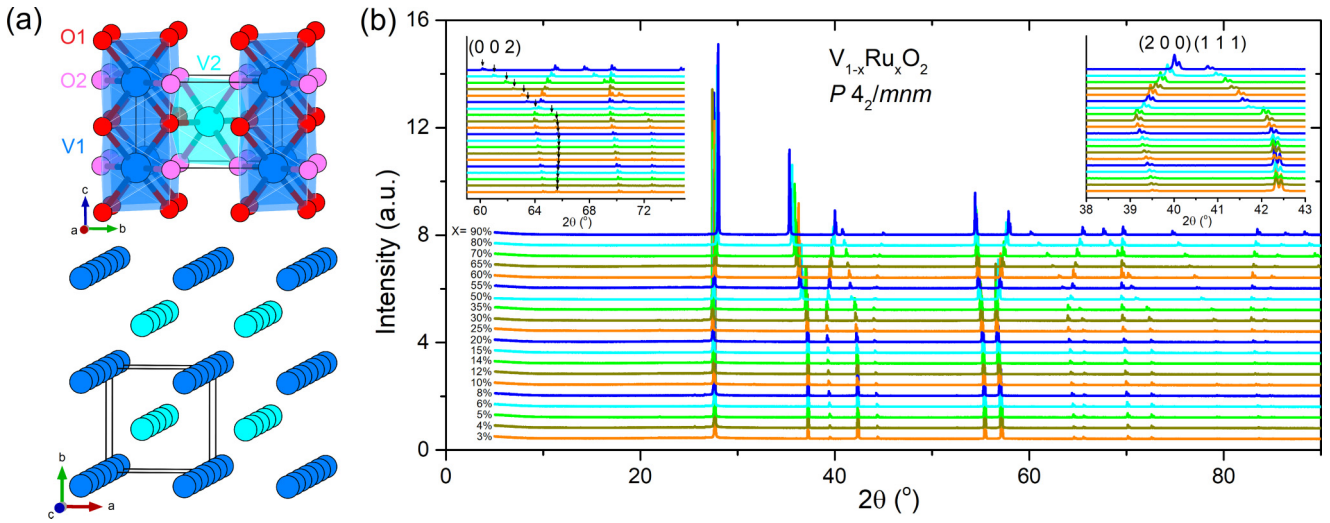

FIG. 1. (a) The crystal structure of $V_{1-x}Ru_xO_2$, where blue and cyan balls represent V atoms, and pink and red balls stand for O atoms. The bottom figure shows the linear chain feature of V in VO_2. (b) (main panel) Powder x-ray diffraction patterns of $V_{1-x}Ru_xO_2$ at 293 K; (inset, left) the trend of (0 0 2) peak position marked by black arrows; and (inset, right) the trends of (2 0 0) and (1 1 1) peak positions.

the PPMS from 2 to 30 K. Samples used for heat capacity measurements were pellets of the powders annealed at 950 °C.

III. RESULTS AND DISCUSSION

A. Crystal structure and phase determination

Undoped VO_2 $>\sim$340 K crystallizes in the rutile structure. This structure has tetragonal symmetry, in space group $P4_2/mnm$ (No. 136) [9,10]. The undoped material undergoes a structural phase transition to monoclinic space group $C2/m$ (No.12)[2] accompanied by a MIT upon cooling $<\sim$340 K. With electron doping, in Mo-doped VO_2 [21], for example, the MIT is suppressed, and the material adopts a tetragonal structure <300 K. The tetragonal structure of VO_2 is shown in Fig. 1(a). Although there is only one crystallographically equivalent site for either V or O in the tetragonal structure, to facilitate comparison with the monoclinic form, we employ different colors to represent both elements. Edge-shared VO_6 octahedra stack along the c axis of the unit cell and form quasi-one-dimensional vanadium chains running parallel to c, as shown at the bottom of Fig. 1(a). The VO_6 octahedra share oxygen atoms on their vertices perpendicular to the chains. The interatomic distances for V1-O2 and V2-O1 are the same, while V1-O1 and V2-O2 have the same bond lengths, and the latter are longer than the former.

Like the case for Mo-doped VO_2, heavily doped $V_{1-x}Ru_xO_2$ also stabilizes the tetragonal structure at room temperature. PXRD patterns of $x = 0.01$ and 0.02 are shown in Fig. S1 in the Supplemental Material (SM) [43]. They have been fitted by the Le Bail method and are found to adopt a triclinic space group P-1 (No. 2). Figure 1(b) presents the PXRD patterns of $V_{1-x}Ru_xO_2$ at ambient temperature with x ranging from 0.03 to 0.90. The obtained patterns are in good agreement with the tetragonal rutile structure. (Results for all compositions are shown in Fig. S2 in the SM [43].) As shown in the insets of Fig. 1(b), the peak positions do not shift monotonically with an increasing amount of dopant. For instance, the (0 0 2) peak shifts slightly to a higher angle when $x \leqslant 0.15$, while it shifts slightly to a lower angle when $0.2 \leqslant x \leqslant 0.3$ and shifts dramatically to a lower angle when $x \geqslant 0.35$. Similar behavior can be found for the (1 1 1) peak, while the opposite trend can be observed for the (2 0 0) peak, which initially shifts to a low angle when $x \leqslant 0.3$ and then to a higher angle when $x > 0.3$. To visualize the changes of the $V_{1-x}Ru_xO_2$ unit cell, lattice parameters obtained from Rietveld fitting are plotted in Figs. 2(a) and 2(b). The results are in good agreement with previously reported lattice parameters [42]. An obvious trend of increasing the length of a, which is directly relevant to the interchain distances, can be seen before $x = 0.3$ followed by a continuous decrease, i.e., an increase of 1.4% compared with the length of a of $V_{0.97}Ru_{0.03}O_2$ is seen. In the meantime, the length of c, which describes the intrachain V-V distances, shows different behavior, initially decreasing for $x \leqslant 0.15$, i.e., a drop of 0.1%, and increases when $x \geqslant 0.20$, i.e., an increase of 9.1% when compared with the length of c for $V_{0.97}Ru_{0.03}O_2$.

For comparison purposes, to determine whether this behavior is seen for other dopants of VO_2, the cell parameters for a different chemical origin of the electron doping, for $V_{1-x}Mo_xO_2$, were extracted from Ref. [21] and plotted in Fig. 2(a). This allows one to determine whether it is the valence electron count (VEC) per atom that primarily impacts the lattice parameters. Unlike the case for $V_{1-x}Ru_xO_2$, a in $V_{1-x}Mo_xO_2$ increases monotonically with increasing Mo content, while c first increases and then drops, which is opposite to what is seen for $V_{1-x}Ru_xO_2$. The trends of c/a and volume of the unit cell for both $V_{1-x}Ru_xO_2$ and $V_{1-x}Mo_xO_2$ are presented in Fig. 2(c). When the VEC per atom is $<5.967\,e^-$/atom ($x < 30\%$ in $V_{1-x}Ru_xO_2$), c/a of $V_{1-x}Ru_xO_2$ decreases with increasing x, the same as $V_{1-x}Mo_xO_2$. Beyond this point, the c/a ratio of $V_{1-x}Ru_xO_2$ increases with higher concentration of Ru. The inset of Fig. 2(c) illustrates the volume of the unit cell with respect to VEC per atom. Consistent with the larger ionic radius of Mo and Ru than V, the volumes of both series of materials increase as the amount of dopant increases. It is clear from the Mo-Ru doping comparison that the VEC per atom

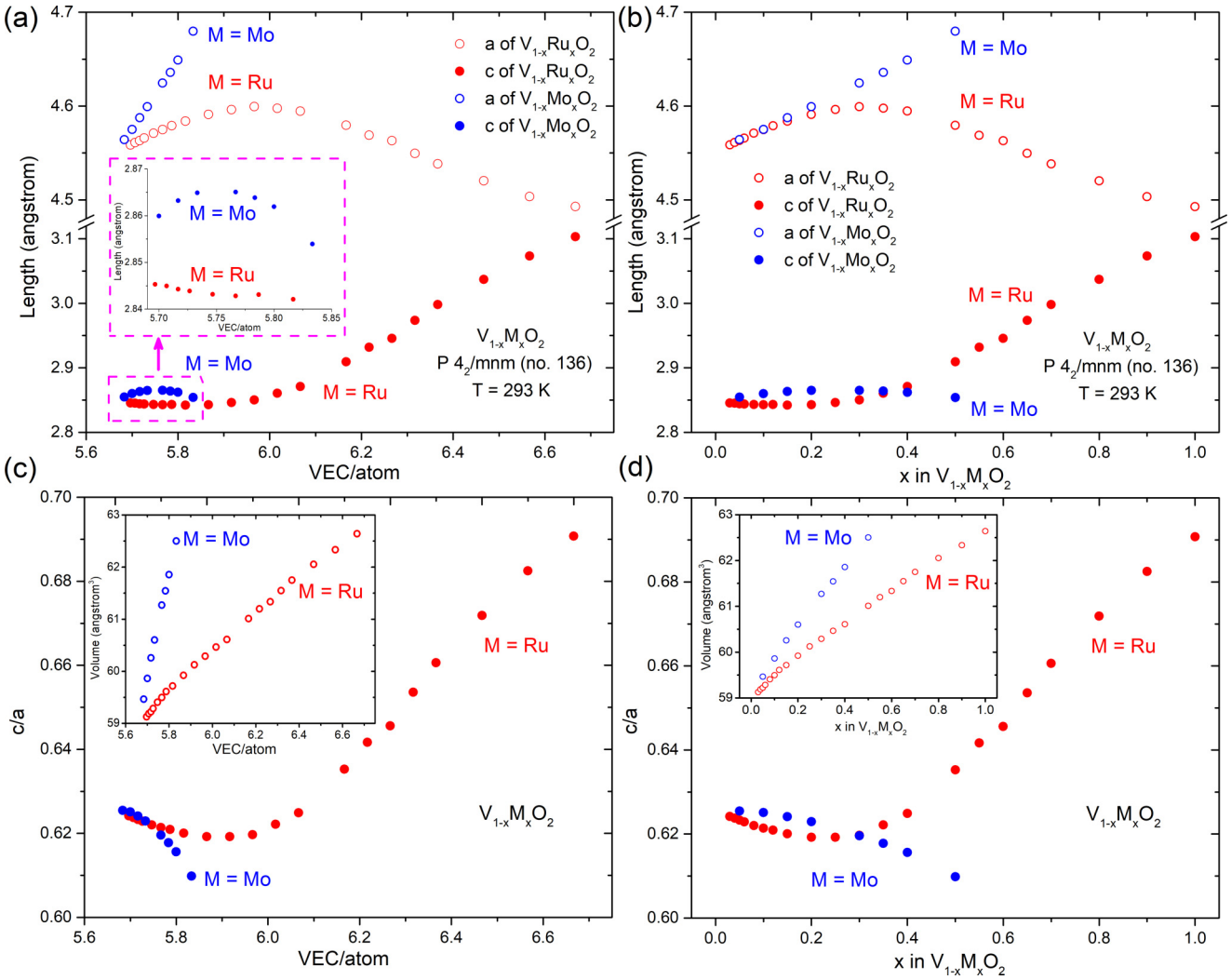

FIG. 2. (a) and (b) (main panel) The lattice dimensions of $V_{1-x}M_xO_2$ (M = Ru or Mo) with respect to (a) valence electron count (VEC) per atom and (b) x in $V_{1-x}M_xO_2$; (inset) zoom-in of the dimension of c in the rutile unit cell for $V_{1-x}M_xO_2$. (c) and (d) (main panel) c/a of $V_{1-x}M_xO_2$ with respect to (c) VEC per atom and (d) x in $V_{1-x}M_xO_2$; (inset) cell volume of $V_{1-x}M_xO_2$ with respect to (c) VEC per atom and (d) x in $V_{1-x}M_xO_2$.

is not the factor that primarily affects the lattice dimensions of $V_{1-x}M_xO_2$. Therefore, we compare the influence of doping value x by comparing the lattice parameters, cell volume, and c/a ratio of $V_{1-x}M_xO_2$, as illustrated in Figs. 2(b) and 2(d). Like what is observed for the VEC per atom case, x (the concentration of dopant) also does not play an essential role in determining lattice dimensions in the doped VO_2 system.

B. Magnetic properties

The general magnetic properties for $V_{1-x}Ru_xO_2$ are shown in Fig. 3. The temperature dependence of the magnetic susceptibility is presented in Fig. 3(a). Sharp transitions reflecting the MIT can be observed >250 K for $x < 0.10$, as shown in the main panel of Fig. 3(a). The transition temperatures are visualized by the peaks of the first derivatives of χT vs T curves shown in the inset. The MITs for $x = 0.01$, 0.02, 0.03, 0.04, 0.05, 0.06, 0.08, and 0.10 are seen at ~327, ~312, ~299, ~289, ~280, ~270, ~255, and ~247 K, which is shown in Fig. 4(a). For $x > 0.1$, no peak can be seen in $d(\chi T)/dT$ vs T since the magnetic susceptibility curves, presented in the top left corner, become smoothly varying with temperature. Interestingly, for $x = 0.01$, the magnetic susceptibility is smaller than that of any other sample immediately below the MIT temperature. This might be because, like the case for undoped VO_2, the formation of the spin singlet below the MIT temperature weakens the magnetic response to an external magnetic field. In Fig. 3(b), the temperature dependence of the inverse magnetic susceptibility (χ^{-1}) <30 K indicates Curie-Weiss-like local moment behavior, and no indication of long-range magnetic ordering can be found. Clear Curie-Weiss behavior can be seen for undoped VO_2 and Mo-doped VO_2 at low temperature, as shown in Ref. [21]. However, by doping Ru atoms onto the V site, the χ^{-1} vs T curves are bent away from the linear fitting for the temperature range from 20 to 30 K, as indicated by the solid lines. The linear fitting is based on the Curie-Weiss law: $1/\chi = T/C - \theta_{CW}/C$, where χ is magnetic susceptibility, θ_{CW} is Curie-Weiss temperature, and C is a constant from which the effective moment ($\mu_{eff} = \sqrt{8C}\ \mu_B$) is derived. Thus, when x increases from

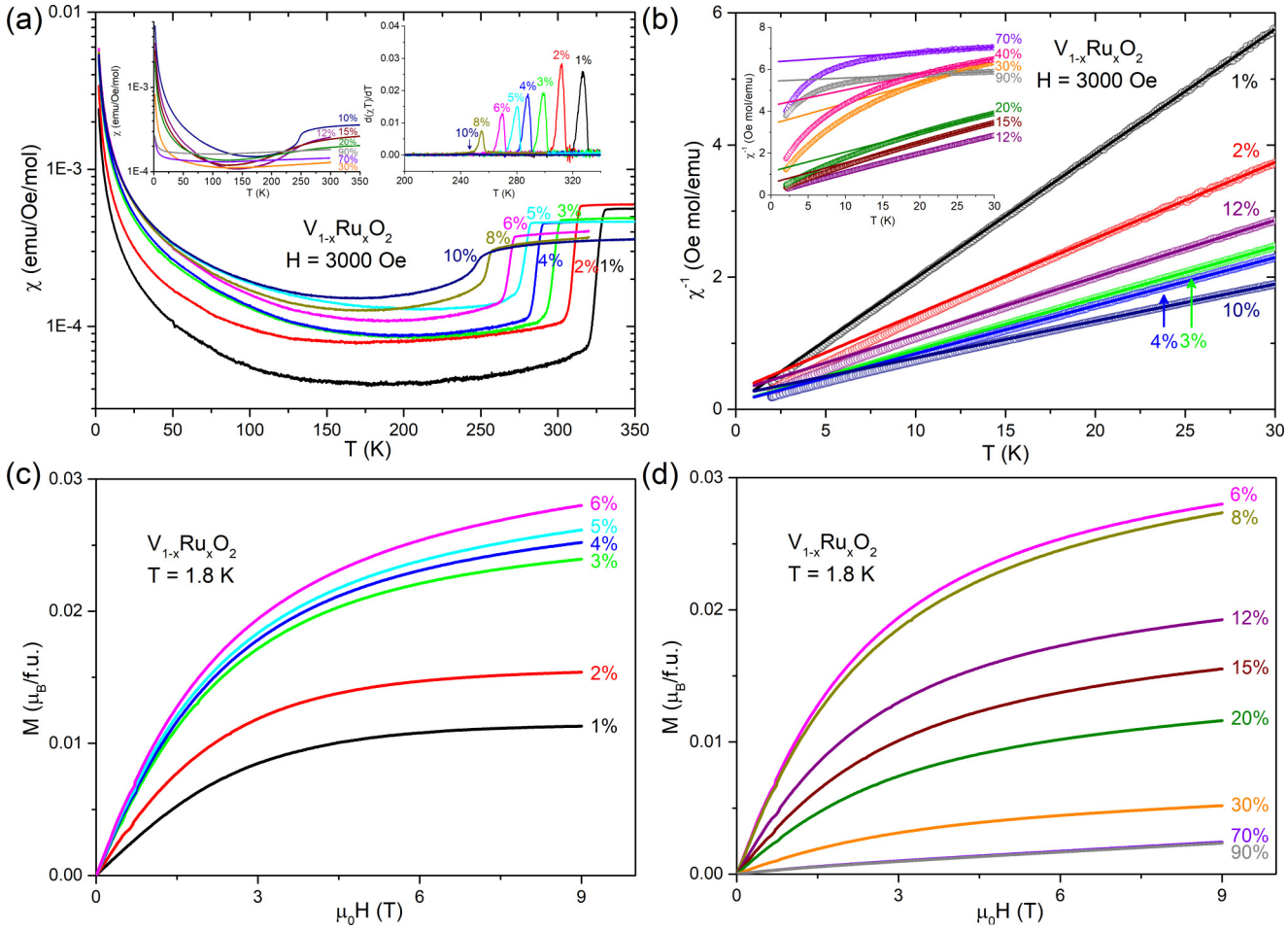

FIG. 3. (a) The temperature-dependence of the magnetic susceptibility of $V_{1-x}Ru_xO_2$ for (main panel) $x \leqslant 10\%$ and (inset, left) $x > 10\%$; (inset, right) $d(\chi T)/dT$ vs T curves. (b) Temperature dependence of inverse magnetic susceptibility for (main panel) $x \leqslant 10\%$ and (inset) $x > 10\%$. The solid lines are linear fittings to the Curie-Weiss law. The field dependence of the magnetization for $V_{1-x}Ru_xO_2$ with (c) $x \leqslant 6\%$ and (d) $x \geqslant 6\%$.

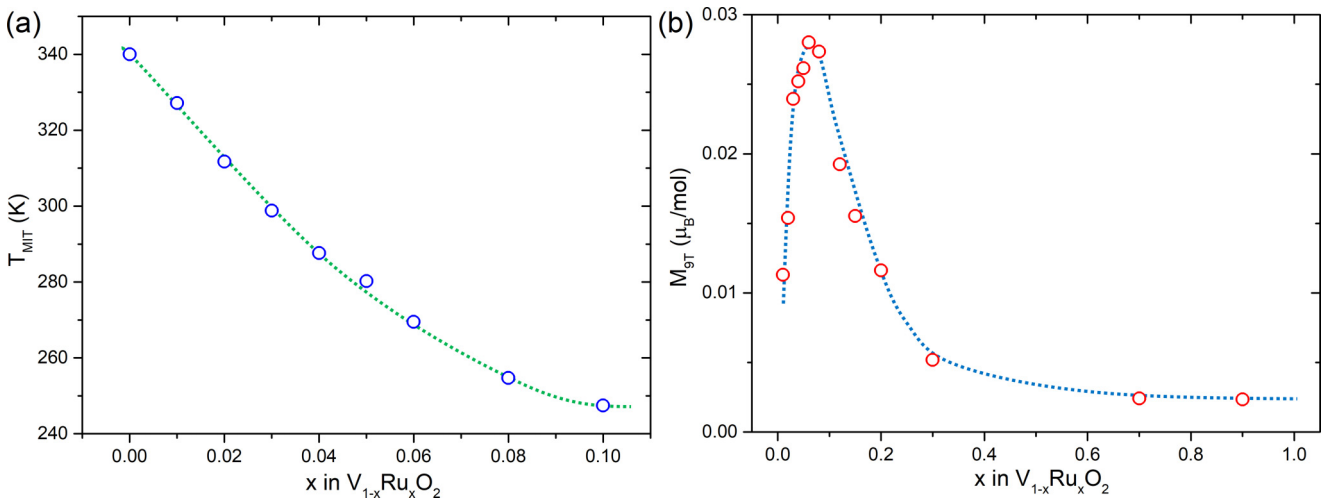

FIG. 4. (a) The trend of the metal-insulator transition (MIT) temperature (T_{MIT}) with respect to x in $V_{1-x}Ru_xO_2$. (b) Molar magnetization at 9 T and 1.8 K with respect to x in $V_{1-x}Ru_xO_2$. The dotted lines in both figures are guides to the eye.

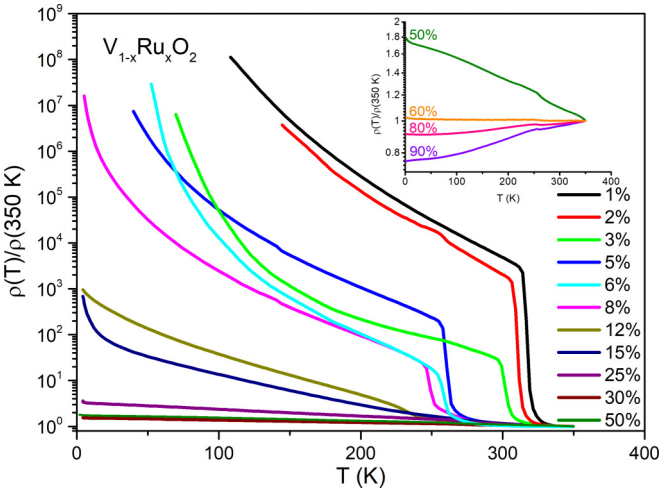

FIG. 5. The temperature dependence of the normalized resistivity of $V_{1-x}Ru_xO_2$ for (main panel) $x \leqslant 50\%$ and (inset) $x \geqslant 50\%$.

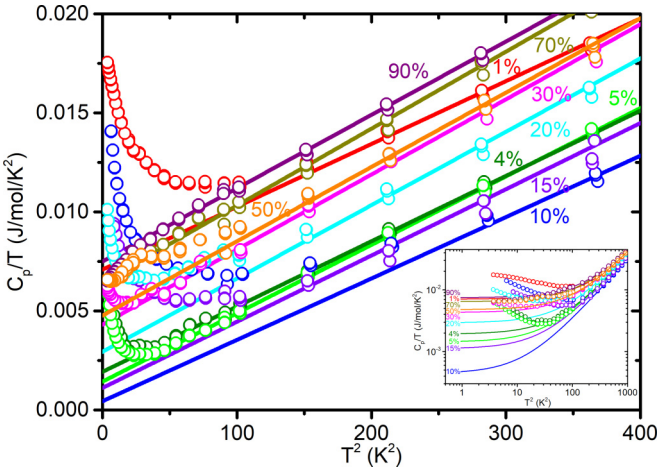

FIG. 6. (main panel) C_p/T vs T^2 curves with a linear scale on both axes. (inset) C_p/T vs T^2 curves with logarithmic scale on both axes. The solid lines are for linear fitting of the higher-temperature data from 400 to 900 K^2 (20–30 K).

0.01 to 0.10, μ_{eff} of $V_{1-x}Ru_xO_2$ increases, and when $0.10 < x \leqslant 0.30$, μ_{eff} drops monotonically then to rise again when $x > 0.30$. In addition, θ_{CW} is negative, ranging from -0.52 (7) K (at $x = 0.01$) to -353 (9) K (for $x = 0.09$), which reveals that antiferromagnetic interactions are dominant in the $V_{1-x}Ru_xO_2$ solid solution in the corresponding temperature range.

The field-dependent magnetization (MH) curves from 0 to 9 T for $V_{1-x}Ru_xO_2$ at 1.8 K are shown in Figs. 3(c) and 3(d). Although the solid solution shows no evidence for long-range magnetic ordering, all the curves are found to bend toward the H axis when the applied magnetic field is large enough, i.e., $\mu_0 H > 2$ T, and exhibit a small unsaturated magnetic moment at 9 T, which is summarized in Fig. 4(b). The MH curves clearly demonstrate that the magnetic moments at 9 T increase with x when $x \leqslant 0.06$ and decrease with x when $x > 0.06$. The linear behavior of MH curves for $x = 0.70$ and 0.90 is closer to what is expected for normal paramagnetic materials.

C. Resistivity

The temperature-dependent resistivity from 1.8 to 300 K in the absence of an applied magnetic field was measured on polycrystalline pellets. Figure 5 presents the temperature dependence of normalized resistivity $[\rho(T)/\rho(350)]$. In the main panel, a sharp increase in resistivity can be found for materials with smaller x values ($x < 0.15$) due to the MIT. The transition temperature is gradually suppressed to lower temperature with larger x, while the MIT cannot be seen in the polycrystalline samples when x reaches 0.15. Thus, the sharp MIT disappears in temperature-dependent resistivity measurements at higher x, but the material remains poorly conducting. Although Ru atoms, which have three more valence electrons than V, are introduced into the system to provide more conducting electrons, the materials persist in their insulating behavior until a surprisingly large doping value. When x increases to 0.50, as shown in the inset of Fig. 5, the material exhibits clear insulating behavior. However, when $x = 60\%$, such insulating behavior is dramatically suppressed, and a metallic resistivity curve is eventually obtained for $x = 80\%$. Thus, low-temperature resistivity measurements down to 0.1 K for $x = 80$ and 90% were carried out; no evidence for bulk superconductivity was observed.

D. Heat capacity

To better probe the electronic behavior of $V_{1-x}Ru_xO_2$, low-temperature heat capacity measurements from 2 to 30 K under no applied magnetic field were performed. The results are presented in Fig. 6. Both axes in the inset are shown on a logarithmic scale for clarity of the data <10 K, while linear scale is used in the main panel. No obvious heat capacity jump corresponding to any kind of phase transition can be seen in the full measured temperature range, which is consistent with the magnetic susceptibility and resistivity measurements. Generally, the heat capacity C_p of materials at low temperature can be represented by $C_p = \gamma T + \beta T^3$, where γ and β reflect the electronic (Sommerfeld coefficient) and phononic contributions, respectively. Thus, a linear fitting for C_p/T vs T^2 curve can be applied to estimate the γ and β in $V_{1-x}Ru_xO_2$, as shown by solid lines in Fig. 6. The intercept of the fitting line with the y axis yields the value of γ. Clearly, when $x \leqslant 10\%$, γ decreases with increasing x from 7.1(2) mJ mol^{-1} K^{-2} ($x = 1\%$) to 0.4(2) mJ mol^{-1} K^{-2} ($x = 10\%$). Furthermore, as x increases from 10 to 90%, γ increases slowly to 7.5 (1) mJ mol^{-1} K^{-2} ($x = 90\%$). For insulators, γ is usually close to zero due to the existence of the bandgap, such as the small γ ($\sim$1.0 mJ mol^{-1} K^{-2}) of undoped VO_2 [21]. Interestingly, although the current materials exhibit insulating behavior when $x < 80\%$, the Sommerfeld coefficient is still growing as x increases. Such behavior indicates that, by introducing more valence electrons into VO_2, the strength of electronic fluctuations varies a lot. Moreover, the low-temperature upturns observed in the heat capacity data can be attributed to Schottky anomalies arising from the fluctuations of the magnetic moments, like what is seen for Mo-doped VO_2 [21].

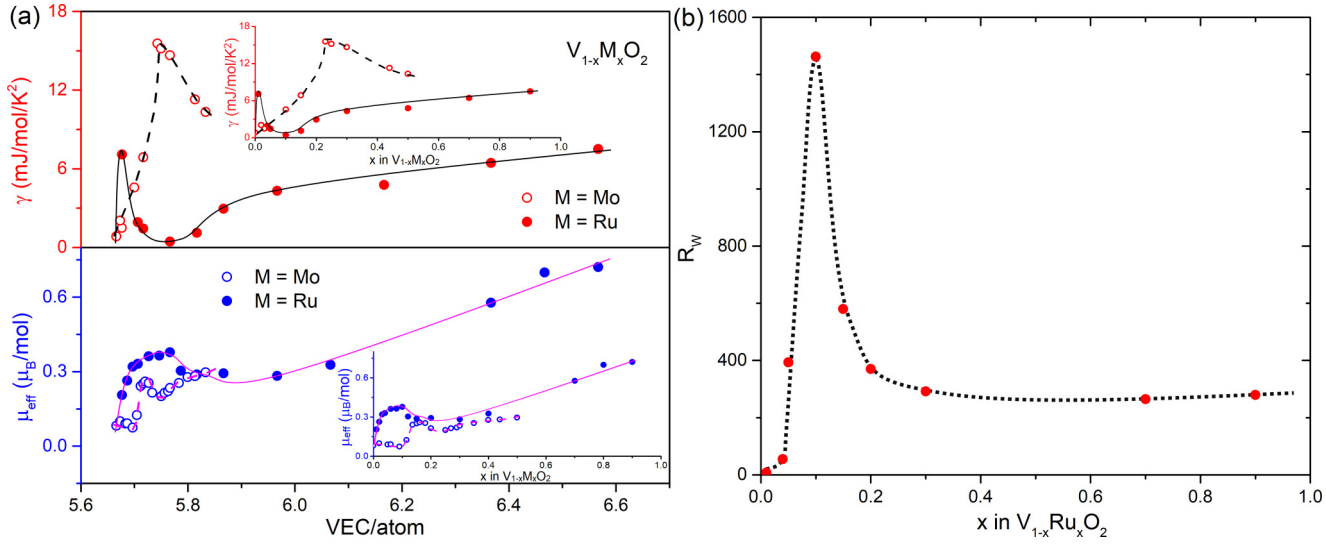

FIG. 7. (a) (upper panel) Sommerfeld coefficient g and (lower panel) effective moment μ_{eff} for $V_{1-x}M_xO_2$ (M = Mo/Ru) with respect to (main panel) valence electron count (VEC) per atom and (inset) x in $V_{1-x}M_xO_2$. The black/magenta solid and dashed lines are guides to the eye. (b) The Wilson ratio of $V_{1-x}Ru_xO_2$. The black dotted line is a guide to the eye.

E. Discussion

To investigate whether the behavior for $V_{1-x}Ru_xO_2$ is like that for another chemically doped VO_2 system $V_{1-x}Mo_xO_2$, a comparison of γ and μ_{eff} for both systems is seen in Fig. 7(a). (The data for the $V_{1-x}Mo_xO_2$ system are extracted from Ref. [21].) The data are shown plotted both as VEC per atom and dopant concentration x per atom. When the VEC per atom hits ~5.77, $V_{1-x}Ru_xO_2$ presents a broad minimum for γ, while $V_{1-x}Mo_xO_2$ has an opposite behavior, i.e., a peak. Moreover, when the doping value changes, a broad minimum of γ appears near $x = 0.10$ for $V_{1-x}Ru_xO_2$, increasing and reaching a peak near $x = 0.23$. For μ_{eff}, a broad maximum emerges at VEC per atom ~5.75 in $V_{1-x}Ru_xO_2$, while for $V_{1-x}Mo_xO_2$, μ_{eff} first drops to a minimum at VEC per atom ~5.7 and then reaches a peak at VEC per atom ~5.72 followed by a valley at VEC per atom ~5.75, which is opposite to what is seen for the Ru counterpart. Furthermore, when the concentration of dopant changes, when $x = 0.10$, $V_{1-x}Ru_xO_2$ exhibits a broad maximum, while $V_{1-x}Mo_xO_2$ shows a minimum.

Different trends between the two systems for both γ and μ_{eff} are observed, which indicates that neither the VEC per atom nor the doping value x are the significant factors that decide the electronic properties of electron-doped VO_2. Therefore, a specific picture is needed to describe how Ru doping can affect the physical properties in $V_{1-x}Ru_xO_2$. Authors of a previous report claim that VO_2 has an electronic configuration where t_{2g} orbitals are formed by one fully filled orbital and two half-filled orbitals instead of two fully filled orbitals which cannot provide unpaired electrons [28]. Thus, with that information in mind, by integrating magnetic and electronic transport behaviors, it can be speculated that, when $x \leqslant 6\%$, the magnetic moment at 9 T increases because Ru brings more electrons into the system and breaks the spin singlet in VO_2 that can suppress the MIT to lower temperature and produce a local magnetic moment. When the doping value increases further to ~10%, the Peierls distortion takes over and starts to become dominant and, thus, makes a small amount of spin-singlet states. This assumption can be evidenced by the Wilson ratio (R_W), defined as $R_W = \frac{4\pi^2\chi_0}{3\gamma}$, where χ_0 is related to the core diamagnetism and temperature-independent paramagnetic contributions such as Pauli paramagnetism and is obtained by fitting temperature-dependent magnetic susceptibility by using modified Curie-Weiss law $\chi = \chi_0 + C/(T - \theta_{CW})$, shown in Fig. 7(b) [44–46]. Here, R_W quantifies the spin fluctuations that enhance the magnetic susceptibility. In $V_{1-x}Ru_xO_2$, R_W starts at ~7.3 when $x = 1\%$ and dramatically increases to ~1460 when $x = 10\%$, dropping gradually to ~300 beyond this point. This means that spin fluctuations become stronger when the Ru doping is <10%, suggesting that the ferromagnetism originates from Ru 4d electrons, considering that $SrRuO_3$ with Ru^{4+} is ferromagnetic [44,46,47].

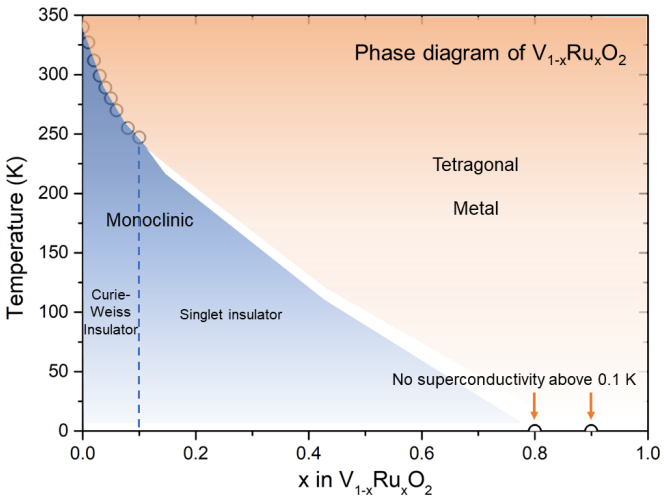

FIG. 8. Proposed electronic phase diagram for $V_{1-x}Ru_xO_2$.

After 10%, the spins start to reform the spin-singlet state, and the magnetization and R_W both drop because of weaker spin fluctuations [44,46]. This process can lead to both insulating behavior and decreasing of the magnetic moment, continuing to $x \sim 80\%$. When $x \geqslant 80\%$, the metallic nature of RuO_2 eventually prevails, resulting in poor metal behavior for heavily doped $V_{1-x}Ru_xO_2$. Thus, we propose a phase diagram for Ru-doped VO_2, shown in Fig. 8. The circles stand for the MIT temperature observed in temperature-dependent magnetic susceptibility. The white area means that the MIT can no longer be observed. With heavier doping of Ru, $V_{1-x}Ru_xO_2$ changes from a Curie-Weiss insulator to a singlet insulator and eventually turns into a metal above $x \sim 80\%$. In the meantime, superconductivity was not observed >0.1 K for metallic samples.

IV. CONCLUSIONS

In this paper, we present the synthesis of a series of materials $V_{1-x}Ru_xO_2$ ($1\% \leqslant x \leqslant 90\%$) using the high-temperature solid-state method. The magnetic properties, electronic transport properties, and heat capacity of selective compositions are investigated. The physical properties of $V_{1-x}Ru_xO_2$ are compared with previously reported $V_{1-x}Mo_xO_2$, and obvious differences can be observed between the two systems as a function of either the VEC per atom or the doping value x, which implies neither of them can be the most significant factor in deciding the electronic/magnetic behavior in electron-doped VO_2. By integrating the magnetic and electronic behaviors and the Wilson ratio, we propose a possible reason for the behavior of $V_{1-x}Ru_xO_2$, but deeper interpretation of the phenomena observed requires further study, such as through the determination of the local structure and further theoretical study of the relationship between itinerant and localized behavior in the rutile structure.

ACKNOWLEDGMENTS

This paper was supported by the Gordon and Betty Moore Foundation, Emergent Phenomena in Quantum Systems initiative, Grant No. GBMF-9066.

[1] M. Imada, A. Fujimori, and Y. Tokura, Metal-insulator transitions, Rev. Mod. Phys. **70**, 1039 (1998).
[2] F. J. Morin, Oxides Which Show a Metal-to-Insulator Transition at the Neel Temperature, Phys. Rev. Lett. **3**, 34 (1959).
[3] M. M. Qazilbash, M. Brehm, B.-G. Chae, P.-C. Ho, G. O. Andreev, B.-J. Kim, S. J. Yun, A. V. Balatsky, M. B. Maple, F. Keilmann *et al.*, Mott transition in VO_2 revealed by infrared spectroscopy and nano-imaging, Science **318**, 1750 (2007).
[4] T. Yao, X. Zhang, Z. Sun, S. Liu, Y. Huang, Y. Xie, C. Wu, X. Yuan, W. Zhang, Z. Wu *et al.*, Understanding the Nature of the Kinetic Process in a VO_2 Metal-Insulator Transition, Phys. Rev. Lett. **105**, 226405 (2010).
[5] S. Biermann, A. Poteryaev, A. I. Lichtenstein, and A. Georges, Dynamical Singlets and Correlation-Assisted Peierls Transition in VO_2, Phys. Rev. Lett. **94**, 026404 (2005).
[6] R. J. O. Mossanek and M. Abbate, Evolution of the $d_{\|}$ band across the metal-insulator transition in VO_2, Solid State Commun. **135**, 189 (2005).
[7] S. Rao Popuri, A. Artemenko, C. Labrugere, M. Miclau, A. Villesuzanne, and M. Pollet, VO_2 (A): Reinvestigation of crystal structure, phase transition and crystal growth mechanisms, J. Solid State Chem. **213**, 79 (2014).
[8] Z. Hiroi, Structural instability of the rutile compounds and its relevance to the metal-insulator transition of VO_2, Prog. Solid State Chem. **43**, 47 (2015).
[9] J. B. Goodenough, The two components of the crystallographic transition in VO_2, J. Solid State Chem. **3**, 490 (1971).
[10] C. N. Berglund and H. J. Guggenheim, Electronic properties of VO_2 near the semiconductor-metal transition, Phys. Rev. **185**, 1022 (1969).
[11] J. B. Goodenough and H. Y.-P. Hong, Structures and a two-band model for the system $V_{1-x}Cr_xO_2$, Phys. Rev. B **8**, 1323 (1973).
[12] A. Zylbersztejn and N. F. Mott, Metal-Insulator transition in vanadium dioxide, Phys. Rev. B **11**, 4383 (1975).
[13] J. P. Pouget, H. Launois, T. M. Rice, P. Dernier, A. Gossard, G. Villeneuve, and P. Hagenmuller, Dimerization of a linear Heisenberg chain in the insulating phases of $V_{1-x}Cr_xO_2$, Phys. Rev. B **10**, 1801 (1974).
[14] J. P. Pouget, H. Launois, J. P. D'Haenens, P. Merenda, and T. M. Rice, Electron Localization Induced by Uniaxial Stress in Pure VO_2, Phys. Rev. Lett. **35**, 873 (1975).
[15] M. Gupta, A. J. Freeman, and D. E. Ellis, Electronic structure and lattice instability of metallic VO_2, Phys. Rev. B **16**, 3338 (1977).
[16] A. Liebsch, H. Ishida, and G. Bihlmayer, Coulomb correlations and orbital polarization in the metal-insulator transition of VO_2, Phys. Rev. B **71**, 085109 (2005).
[17] R. M. Wentzcovitch, W. W. Schulz, and P. B. Allen, VO_2: Peierls or Mott-Hubbard? A View from Band Theory, Phys. Rev. Lett. **72**, 3389 (1994).
[18] M. W. Haverkort, Z. Hu, A. Tanaka, W. Reichelt, S. V. Streltsov, M. A. Korotin, V. I. Anisimov, H. H. Hsieh, H.-J. Lin, C. T. Chen *et al.*, Orbital-Assisted Metal-Insulator Transition in VO_2, Phys. Rev. Lett. **95**, 196404 (2005).
[19] M. S. Laad, L. Craco, and E. Müller-Hartmann, Metal-insulator transition in rutile-based VO_2, Phys. Rev. B **73**, 195120 (2006).
[20] J. M. Tomczak, F. Aryasetiawan, and S. Biermann, Effective bandstructure in the insulating phase versus strong dynamical correlations in metallic VO_2, Phys. Rev. B **78**, 115103 (2008).
[21] K. L. Holman, T. M. McQueen, A. J. Williams, T. Klimczuk, P. W. Stephens, H. W. Zandbergen, Q. Xu, F. Ronning, and R. J. Cava, Insulator to correlated metal transition in $V_{1-x}Mo_xO_2$, Phys. Rev. B **79**, 245114 (2009).
[22] W. Rüdorff and J. Märklin, Untersuchungen an ternären oxiden der Übergangsmetalle. III. Die rutilphase $(V_{1-x}Nb_x)O_2$, Z. Für Anorg. Allg. Chem. **334**, 142 (1964).
[23] G. Villeneuve, A. Bordet, A. Casalot, J. P. Pouget, H. Launois, and P. Lederer, Contribution to the study of the metal-insulator

transition in the $V_{1-x}Nb_xO_2$ system: I—crystallographic and transport properties, J. Phys. Chem. Solids **33**, 1953 (1972).

[24] J. P. Pouget, P. Lederer, D. S. Schreiber, H. Launois, D. Wohlleben, A. Casalot, and G. Villeneuve, Contribution to the study of the metal-insulator transition in the $V_{1-x}Nb_xO_2$ system—II magnetic properties, J. Phys. Chem. Solids **33**, 1961 (1972).

[25] D. Mikhailova, N. N. Kuratieva, Y. Utsumi, A. A. Tsirlin, A. M. Abakumov, M. Schmidt, S. Oswald, H. Fuess, and H. Ehrenberg, Composition-dependent charge transfer and phase separation in the $V_{1-x}Re_xO_2$ solid solution, Dalton Trans. **46**, 1606 (2017).

[26] X. Tan, T. Yao, R. Long, Z. Sun, Y. Feng, H. Cheng, X. Yuan, W. Zhang, Q. Liu, C. Wu, Y. Xie, and S. Wei, Unraveling metal-insulator transition mechanism of VO_2 triggered by tungsten doping, Sci. Rep. **2**, 466 (2012).

[27] I.-H. Hwang, Z. Jin, C.-I. Park, and S.-W. Han, The influence of structural disorder and phonon on metal-to-insulator transition of VO_2, Sci. Rep. **7**, 14802 (2017).

[28] T. Berlijn, P. C. Snijders, O. Delaire, H.-D. Zhou, T. A. Maier, H.-B. Cao, S.-X. Chi, M. Matsuda, Y. Wang, M. R. Koehler *et al.*, Itinerant Antiferromagnetism in RuO_2, Phys. Rev. Lett. **118**, 077201 (2017).

[29] Z. H. Zhu, J. Strempfer, R. R. Rao, C. A. Occhialini, J. Pelliciari, Y. Choi, T. Kawaguchi, H. You, J. F. Mitchell, Y. Shao-Horn *et al.*, Anomalous Antiferromagnetism in Metallic RuO_2 Determined by Resonant X-Ray Scattering, Phys. Rev. Lett. **122**, 017202 (2019).

[30] X. Chen, J. Li, and Q. Lv, Thermoelectrical and optical characteristics research on novel nanostructured VO_2 thin film, Optik **124**, 2041 (2013).

[31] H. Guo, K. Chen, Y. Oh, K. Wang, C. Dejoie, S. A. Syed Asif, O. L. Warren, Z. W. Shan, J. Wu, and A. M. Minor, Mechanics and dynamics of the strain-induced M1–M2 structural phase transition in individual VO_2 nanowires, Nano Lett. **11**, 3207 (2011).

[32] E. Strelcov, Y. Lilach, and A. Kolmakov, Gas sensor based on metal-insulator transition in VO_2 nanowire thermistor, Nano Lett. **9**, 2322 (2009).

[33] C. Si, W. Xu, H. Wang, J. Zhou, A. Ablat, L. Zhang, J. Cheng, Z. Pan, L. Fan, C. Zou, and Z. Wu, Metal-insulator transition in $V_{1-x}W_xO_2$: Structural and electronic origin, Phys. Chem. Chem. Phys. **14**, 15021 (2012).

[34] J. Jeong, N. Aetukuri, T. Graf, T. D. Schladt, M. G. Samant, and S. S. P. Parkin, Suppression of metal-insulator transition in VO_2 by electric field–induced oxygen vacancy formation, Science **339**, 1402 (2013).

[35] G. Stefanovich, A. Pergament, and D. Stefanovich, Electrical switching and Mott transition in VO_2, J. Phys. Condens. Matter **12**, 8837 (2000).

[36] M. Liu, H. Y. Hwang, H. Tao, A. C. Strikwerda, K. Fan, G. R. Keiser, A. J. Sternbach, K. G. West, S. Kittiwatanakul, J. Lu *et al.*, Terahertz-field-induced insulator-to-metal transition in vanadium dioxide metamaterial, Nature (London) **487**, 345 (2012).

[37] J. I. Sohn, H. J. Joo, D. Ahn, H. H. Lee, A. E. Porter, K. Kim, D. J. Kang, and M. E. Welland, Surface-stress-induced Mott transition and nature of associated spatial phase transition in single crystalline VO_2 nanowires, Nano Lett. **9**, 3392 (2009).

[38] J. Cao, W. Fan, Q. Zhou, E. Sheu, A. Liu, C. Barrett, and J. Wu, Colossal thermal-mechanical actuation via phase transition in single-crystal VO_2 microcantilevers, J. Appl. Phys. **108**, 083538 (2010).

[39] S. Shin, S. Suga, M. Taniguchi, M. Fujisawa, H. Kanzaki, A. Fujimori, H. Daimon, Y. Ueda, K. Kosuge, and S. Kachi, Vacuum-ultraviolet reflectance and photoemission study of the metal-insulator phase transitions in VO_2, V_6O_{13}, and V_2O_3, Phys. Rev. B **41**, 4993 (1990).

[40] T. C. Koethe, Z. Hu, M. W. Haverkort, C. Schüßler-Langeheine, F. Venturini, N. B. Brookes, O. Tjernberg, W. Reichelt, H. H. Hsieh, H.-J. Lin *et al.*, Transfer of Spectral Weight and Symmetry Across the Metal-Insulator Transition in VO_2, Phys. Rev. Lett. **97**, 116402 (2006).

[41] U. Schwingenschlögl and V. Eyert, The vanadium magnéli phases V_nO_{2n-1}, Ann. Phys. **516**, 475 (2004).

[42] J. Arnold, J. Feller, and U. Steiner, Chemischer transport fester lösungen $V_{1-x}Ru_xO_2$ und $V_{1-x}Os_xO_2$, Z. Für Anorg. Allg. Chem. **634**, 2026 (2008).

[43] See Supplemental Material at http://link.aps.org/supplemental/10.1103/PhysRevMaterials.6.075005 for powder XRD patterns for 1 and 2% Ru-doped VO2 with Le Bail fitting and powder XRD patterns for ($x \geqslant 3\%$) with Rietveld fitting.

[44] K. G. Wilson, The renormalization group: critical phenomena and the Kondo problem, Rev. Mod. Phys. **47**, 773 (1975).

[45] Z. Fisk, H. R. Ott, and G. Aeppli, Experimental perspectives on heavy-electron metals, Jpn. J. Appl. Phys. **26**, 1882 (1987).

[46] P. Prelovšek, K. Morita, T. Tohyama, and J. Herbrych, Vanishing Wilson ratio as the hallmark of quantum spin-liquid models, Phys. Rev. Research **2**, 023024 (2020).

[47] J. M. Longo, P. M. Raccah, and J. B. Goodenough, Magnetic properties of $SrRuO_3$ and $CaRuO_3$, J. Appl. Phys. **39**, 1327 (1968).